Volume-of-interest cone-beam CT using a 2.35 MV beam generated with a carbon target

James L. Robar[a)]
Department of Radiation Oncology and Department of Physics and Atmospheric Science, Dalhousie University, 5820 University Avenue, Halifax, Nova Scotia B3H 1V7, Canada

David Parsons
Department of Physics and Atmospheric Science, Dalhousie University, Halifax, Nova Scotia B3H 1V7, Canada

Avery Berman
Nova Scotia Cancer Centre, Capital District Health Authority, Halifax, Nova Scotia B3H 1V7, Canada

Alex MacDonald
Department of Physics and Atmospheric Science, Dalhousie University, Halifax, Nova Scotia B3H 1V7, Canada

Purpose: This is a proof-of-concept study addressing volume of interest (VOI) cone beam CT (CBCT) imaging using an x-ray beam produced by 2.35 MeV electrons incident on a carbon linear accelerator target. Methodology is presented relevant to VOI CBCT image acquisition and reconstruction. Sample image data are given to demonstrate and compare two approaches to minimizing artifacts arising from reconstruction with truncated projections. Dosimetric measurements quantify the potential dose reduction of VOI acquisition relative to full-field CBCT. The dependence of contrast-to-noise ratio (CNR) on VOI dimension is investigated.
Methods: A paradigm is presented linking the treatment planning process with the imaging technique, allowing definition of an imaging VOI to be tailored to the geometry of the patient. Missing data in truncated projection images are completed using *a priori* information in the form of digitally reconstructed radiographs (DRRs) generated from the planning CT set. This method is compared to a simpler technique of extrapolating truncated projection data prior to reconstruction. The utility of these approaches is shown through imaging of a geometric phantom and the head-and-neck section of a lamb. The total scatter factor of the 2.35 MV/carbon beam on field size is measured and compared to a standard therapeutic beam to estimate the comparative dose reduction inside the VOI. Thermoluminescent dosimeters and Gafchromic film measurements are used to compare the imaging dose distributions for the 2.35 MV/carbon beam between VOI and full-field techniques. The dependence of CNR on VOI dimension is measured for VOIs ranging from 4 to 15 cm diameter.
Results: Without compensating for missing data outside of truncated projections prior to reconstruction, pronounced boundary artifacts are present, in three dimensions, within 2–3 cm of the edges of the VOI. These artifacts, as well as cupping inside the VOI, can be reduced substantially using either the DRR filling or extrapolation techniques presented. Compared to 6 MV, the 2.35 MV/carbon beam shows a substantially greater dependence of total scatter factor on field size, indicating a comparative advantage of the VOI approach when combined with the low-Z target beam. Dosimetric measurements in the anthropomorphic head phantom demonstrate a dose reduction by up to 15% and 75% inside and outside of the VOI, respectively, compared to full-field imaging. For the 2.35 MV/carbon beam, CNR was shown to be approximately invariant with VOI dimension for bone and lung objects.
Conclusions: The low-Z target, VOI CBCT technique appears to be feasible and combines the desirable characteristics of the low-Z target beam with regard to CNR, with the capacity to localize the imaging dose to the anatomy relevant to the image guidance task. © *2012 American Association of Physicists in Medicine*. [http://dx.doi.org/10.1118/1.4728977]

Key words: low-Z target, carbon, volume-of-interest, region-of-interest, cone beam CT

I. INTRODUCTION

Over the past few years, several investigators have demonstrated the concept of using low atomic number (Z) linear accelerator targets to produce x-ray beams with energy characteristics suited to imaging. Replacement of the conventional tungsten/copper therapy target with one composed of beryllium,[1,2] carbon,[3–6] diamond,[7] or aluminum,[2,8] and re-

moval of flattening filtration allows the recovery of a significant component of photons in the diagnostic energy range. The energy of the electron beam incident on the target may also be lowered compared to that used for therapeutic photon or electron beams,[8] which serves to further increase the relative proportion of diagnostic energy photons in the spectrum. The modification of the photon spectrum enhances

differential attenuation in patient tissues thereby improving contrast, and the approach may be coupled with use of a higher efficiency detector for further improvement of contrast-to-noise (CNR) in imaging.[6,9] While the degree of improvement in image quality depends on the beam line and detector designs, we have shown previously, for example, that compared to 6 MV imaging, use of a 3.5 MeV electron beam incident on an aluminum target yields an improvement of CNR by factors ranging from 2.7 to 4.3 in cone beam CT (CBCT) images. Alternatively, for the same CNR, imaging dose may be reduced approximately by a factor of ~8.[8] The markedly improved image quality introduces a number of possible advantages and applications. For example, the method provides a streamlined option for improving planar or CBCT image quality without the cost, complexity, and quality assurance associated with an auxiliary onboard imaging (OBI) system. Unlike a kV beam line orthogonal to the treatment beam axis, the low-Z target beam line allows beam's-eye-view imaging with improved image quality compared that obtained with a conventional MV beam.

Also unlike kV OBI systems, a low-Z target beam line will usually include a multileaf collimator (MLC). This is central to the focus of this paper, in which we examine the possibility of combining the low-Z target beam with dynamic control of the MLC during CBCT acquisition, in order to capture only the "volume-of-interest" required for a particular image guidance task. There are several potential benefits of this concept. First, by using customized collimation to define a desired VOI, three-dimensional image data of the relevant anatomy, e.g., the target volume, may be acquired while minimizing imaging dose to peripheral tissues. Reduction of peripheral imaging dose remains a key issue in low-Z target imaging, given that, for the same CNR the dose may be ~70 times that for kV CBCT.[6] Second, while some kV CBCT OBI systems offer a "spotlight" technique where the kV collimators reduce the projected field dimension, this mode is inflexible in that it requires the imaged volume to be located on the axis of rotation. In comparison, application of a dynamic MLC sequence should accommodate an arbitrarily located VOI, and in concept, other options such as capturing multiple imaging volumes in a single acquisition. Third, compared to full-field imaging, use of an MLC-collimated beam to reduce the field size may improve the primary-to-scatter characteristics in the imaging beam.[10] We note that precedents for VOI CBCT exist in the contexts of diagnostic imaging or guidance during therapy. For example, recently Chen *et al.*[11] applied a fixed copper mask to collimate a 80 kVp beam for mammographic applications, demonstrating marked improvement of CNR, with more than a five-fold reduction of peripheral dose. With the goal of image guidance during lung radiotherapy, Ford *et al.*[12] acquired projections from an arc of conformal treatment beam apertures. However, in contrast to the present work, a standard 6 MV beam was used and the imaging dose was that of the treatment fraction itself, i.e., on the order of 2 Gy.

In this study, we employ an x-ray beam generated by 2.35 MeV electrons incident on a carbon target to demonstrate the concept and feasibility of low-Z target VOI CBCT imaging. A workflow is proposed wherein the VOI is defined at the time of treatment planning and executed on the linear accelerator. The challenge of image reconstruction using MLC-truncated projections is addressed and a method for minimizing truncation artifact is proposed. Dose reduction, relative to full-field CBCT, is quantified through measurement and the variation of CNR with VOI dimension is examined.

II. METHODS AND MATERIALS

II.A. Low-Z target beam production

The low-Z target was installed in the linear accelerator (21EX, Varian Medical Systems) as described previously;[8] however, the beam line has been refined in several respects. First, the target material has been changed from aluminum to carbon, primarily for its higher melting point. The target itself, a disk 7.6 mm thick, was installed in a fabricated bushing similar to that used to hold an electron scattering foil. In order to minimize focal spot dimension,[2] the upper surface of the target was offset from the carousel surface to locate it as close as possible to, and in this case 9 mm below the lower surface of the beryllium exit window of the primary collimator. Other than the monitor unit chamber and Mylar window, no additional attenuating material was present in the beam line. The linac was operated in electron mode using a dedicated program board; however, compared to the our previous setup,[8] the bending magnet shunt current was adjusted to lower the mean electron energy from 3.5 MeV to 2.35 MeV (and henceforth this beam is referred to as 2.35 MV/carbon.) This energy adjustment was done based on the significant improvement of CNR with reduced energy reported previously.[8] Since beam current was observed to diminish with reduced mean electron energy, once the bending magnet shunt current was set, the electron gun current, grid voltage, and solenoid/buncher steering coil set points were tuned carefully in order to generate, with the carbon target in place, a dose rate allowing a 2.35 MV/carbon CBCT acquisition to be completed in several minutes. For the beam used in this study, for example, a 10 cm × 10 cm field at depth of 5 cm and source-to-axis distance (SAD) of 100 cm gives a dose rate of 0.7 cGy/min, and 1 MU corresponds to 0.8 mGy. The imaging system allows specification of cMU precision, facilitating fine control of the dose per projection. Note that, while it was possible to further reduce the energy below 2.0 MeV, at least in electron mode this would have required significantly longer acquisition times. Although linac manufacturer specifications relate bending magnet shunt current to electron energy, as described previously,[13] the energy of the electron beam was confirmed by replacing the carbon target with a 4 MeV scattering foil and measuring the electron percent depth dose with an electron diode. This result was then compared with a corresponding Monte Carlo modeled PDD, where the model energy was tuned to match the measurement—confirming agreement with the manufacturer's specifications.

II.B. VOI CBCT acquisition

CBCT imaging was performed using a benchtop system similar to that described previously,[8] in which the object is
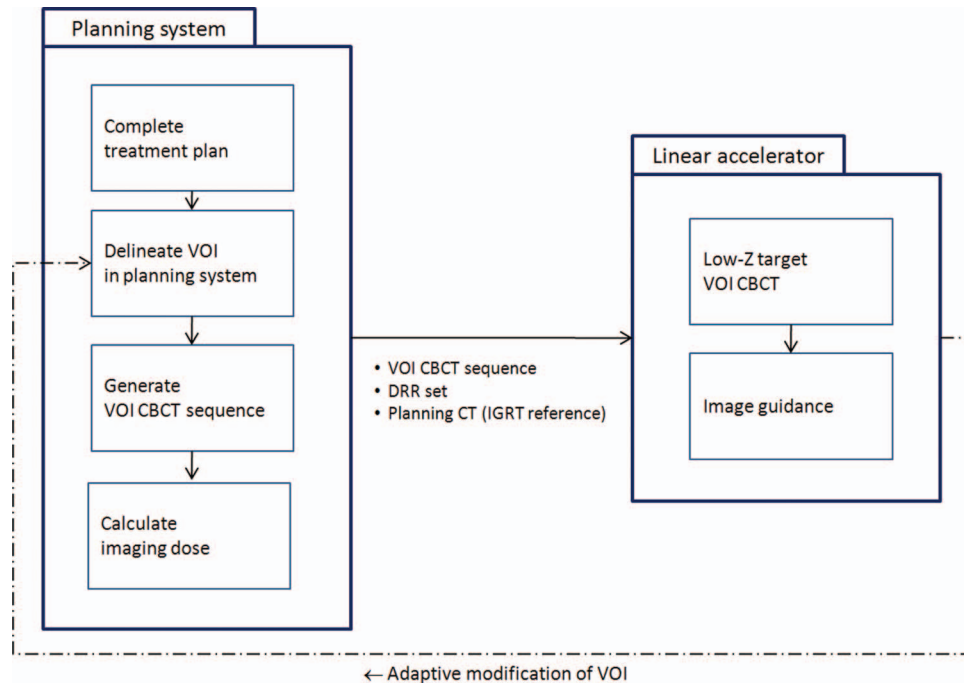
FIG. 1. Workflow for low-Z target volume-of-interest CBCT. A VOI defined in the planning system establishes dynamic arc sequence used in imaging and also provides DRR information used to complete data in truncated projections.

placed on a computer-controlled rotation stage with low-Z target beam axis oriented horizontally and intersecting the rotation axis. The amorphous silicon imaging panel, with an array of 1024 × 768 photodiodes and 40 cm × 30 cm area (IDU20, Varian Medical, Inc.) was supported vertically and orthogonal to the beam axis. The panel was not modified in any way with regard to its buildup or detector layers, and the usual copper conversion layer was in place for all imaging. The stage was rotated at a constant angular velocity, while projection images were acquired in continuous mode using the imaging acquisition system (IAS3) software. Upon acquiring each projection, the stage angle was recorded for subsequent use during reconstruction. The imaging dose was set by specifying the cMU per projection on the IAS3 workstation, with a possible range of 0.01 MU–4.09 MU. VOI CBCT requires synchronization in addition to that previously described, i.e., the rotation angle, elapsed MUs (which also controls the number of projections acquired) and MLC leaf positions must all be correlated. The dynamic MLC file, which is generated by the planning system (see below) and describes leaf positions as a fraction of total MUs elapsed, is loaded by the MLC workstation prior to the acquisition. Since the rate of leaf motion is controlled by the total MU set on the linac console, this parameter must be specified to equal to (number of projections) × (cMU per projection); this ensures that as the final projection has been acquired, MLC leaves have completed their trajectories. For the CBCT imaging presented in this work, 233 projections were acquired during a full rotation of 360° (1.55° per projection).

II.C. Definition of the VOI and imaging protocol

A potential advantage of the VOI approach, aside from the benefit of dose reduction, is the opportunity to define a cus-

tomized imaging protocol at the time of treatment planning. A possible paradigm is illustrated in Fig. 1, in which, upon completion of the treatment plan, a three-dimensional VOI is designed as appropriate to the planning geometry. For example, the VOI may be formed by a simple expansion of the planning target volume (PTV), or extended to also encompass particular proximal structures to aid in image guidance. In the planning system used here (Eclipse 8.9, Varian Medical Systems) a dynamic arc is added to the treatment plan, wherein the MLC adapts to conform to the VOI projection throughout the rotation. The angular range of this arc is definable, but typically would be at least 180° plus the cone angle, and for all studies herein, we used a full 360° arc. Although not the topic of this paper, definition of the imaging protocol at the time of treatment planning also presents the possibility of calculation of the imaging dose and incorporation into the plan. At the completion of this process, three datasets are forwarded from the planning system to the console/imaging workstation at the treatment unit: (i) the MLC sequence for imaging, (ii) the planning CT (to serve as a reference in image guidance), and (iii) a set of digitally reconstructed radiographs (DRRs), used to fill missing data in truncated projections prior to reconstruction as explained below. With regard to (i), since the planning system will produce an "arc dynamic" sequence describing MLC apertures as a function of gantry angle, for the benchtop CBCT acquisition used here, this is converted to a "dose dynamic" sequence specifying a fixed gantry and a series of MLC apertures as a function of fractional MUs elapsed.

II.D. Reconstruction from MLC-truncated projections

Reconstruction from truncated CBCT projections, with the widely employed Feldkamp Davis Kress (FDK) algorithm[14]
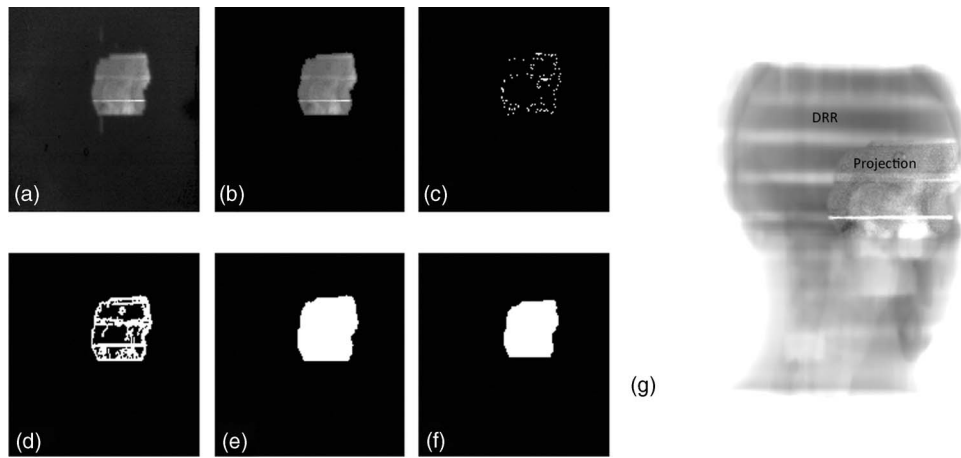
FIG. 2. Process of identifying the truncated projection data and merging with DRR image data. Truncated projection data (a) are thresholded (b), Canny-filtered (c), dilated and filled (d) and (e), then eroded (f). The data in the identified aperture are then combined with DRR data scaled through a linear fit to produce the composite image (g).

is problematic, resulting in boundary-ring and cupping artifacts.[15] Various approaches have been taken to address these issues, including for example, extrapolating projection data outside of the truncated image,[16] filling missing data from sparsely acquired full-field projections,[17] equalizing intensity inside and outside of the truncated projection,[18] or reconstruction using backprojection-filtration methods.[19] Ruchala *et al.* recognized that the radiation oncology paradigm usually provides *a priori* information in the form of a planning CT, which may be used to fill in a fan beam MVCT sinogram.[20] In the present work, we compare two possible approaches. First, we examine a method of filling data outside of the truncated projection using data arising from the patient's planning CT. Second, we test a comparatively simplistic method whereby truncated projections are extrapolated beyond the collimation of the MLC.

The DRR filling method we have employed is similar to the work of Ruchala with regard to its use of pre-existing image data. Here, the planning CT is used to produce set of DRRs within the planning system at discrete angles throughout the gantry arc corresponding to the image acquisition. A full-field DRR is generated for every 2° of arc rotation by adding a single template of static beams, and these DRRs are exported to the reconstruction software (Fig. 1). Prior to filtration and backprojection, as detailed in Fig. 2, an estimate of the missing data in the raw truncated projection is completed as follows: (a) thresholding is applied to eliminate image features such as interleaf leakage and low intensity noise, yielding (b). Canny filtration is applied to detect edges (c) and dilation is performed on this binary image to ensure continuity of the detected aperture (d). Holes are filled (e) and the result is eroded to finalize a mask matching the original aperture dimension (f). Next, the DRR corresponding to the gantry angle closest to that of the truncated projection is selected and resized according to the magnification of the projection. Pixel values in the DRR image are scaled to the acquired projection by establishing a linear fit between intensity values surrounding the inner (projection side) and outer (DRR side) circumference of the mask. After the DRR image is scaled, it is masked using

(f) and the result is added to the truncated image data in (b). An example of the combined image is shown in (g). After all truncated projections are filled using this technique, standard FDK reconstruction is performed as described previously.[8]

For several reasons, we do not expect that the match between DRR and projection data will be exact. First, the CT and low-Z VOI CBCT are acquired in two different sessions, potentially causing misregistration or deformation between image sets. Second, the DRR reconstruction algorithm available in the planning system will generally not model attenuation by the 2.35 MV/carbon beam. Third, while the DRRs are produced at fixed, regular increments throughout the rotation, the CBCT projections are acquired continuously throughout rotation and may not correspond to the same angles. While these issues are technically surmountable and the process described above could be further refined, the results by Ford,[12] MacDonald,[17] and Kadrmas[16] demonstrate that the effectiveness of filling methods in reducing truncation artifact, for most anatomical sites, is not sensitive in this regard.

The DRR filling method is feasible because the DRR data exist in the radiotherapy paradigm and are readily generated by the planning system. However, the technique relies on provision of an additional dataset that the user or system must store and provide as input. In addition, computational overhead will arise from the steps illustrated in Fig. 2. Therefore, we examined a competing approach of simply extrapolating data beyond the boundary of the truncated region, with a function matched at the boundary location and allowing the projection data to fall off smoothly. Specifically, for each row of the acquired projection image P, a row of the modified image P' is calculated using,

$$P'(u) = P(ubound_{lt}) \frac{1 - e^{-ku}}{1 - e^{-k\,ubound_{lt}}} \quad \text{if } u < ubound_{lt}, \quad (1)$$

$$P'(u) = P(ubound_{rt}) \frac{1 - e^{-k(udim - u)}}{1 - e^{-k(udim - ubound_{rt})}} \quad \text{if } u > ubound_{rt}, \quad (2)$$

$$P'(u) = P(u) \quad \text{if } u \geq ubound_{lt} \text{ and } u \leq ubound_{rt}, \quad (3)$$

where u is the horizontal pixel index, $ubound_{lt}$ and $ubound_{rt}$ are the detected left and right locations of the boundaries of the truncated projection image P and $udim$ is the u-dimension of the projection image P. Note that locations $ubound_{lt}$ and $ubound_{rt}$ are determined following thresholding, e.g., based on a projection such as that shown in Fig. 2(b). The parameter k, controlling the rate of apodization of the data, was set to 0.02 in all cases. Note that the functions of Eqs. (1) and (2) match pixel values at the periphery, but not necessarily the local gradient of the image. However, the gradient at the truncation boundary, between the projection data and the function extending these data, did not introduce content at spatial frequencies higher than in the acquired projection data, when realistic subjects were imaged (e.g., the lamb head-and-neck section, as described below).

II.E. Evaluation of projection filling techniques

Two objects were imaged with the 2.35 MV/carbon beam to demonstrate the severity of the truncation artifact and the degree to which the filling techniques improve the image data. To clearly visualize truncation artifacts, a simple cylindrical CNR phantom, 19 cm in diameter, was imaged with a centered, MLC-defined cylindrical VOI, 12 cm in diameter and 5 cm in length. The second subject was the head-and-neck section of a lamb, with approximate dimensions of 15 cm (lateral) $\times$ 25 cm (anterioposterior). For this subject, an off-axis VOI was defined in the planning system ($\sim 7 \times 7 \times 7$ cm^3, see Fig. 3) and the dynamic MLC tracked this VOI during acquisition. For both subjects, a full-field acquisition was also acquired with a field size of 23 cm $\times$ 30 cm, for comparison.

II.F. Dose reduction with low-Z target VOI CBCT

While it is intuitive that collimating the imaging beam by a dynamic MLC sequence should substantially lower the dose outside of the VOI, the dose inside the VOI itself should be reduced as well, due to a lowered contribution from scattered photons. Assuming a large subject, this should be described by the dependence of the total scatter factor (S_{total}) on field size, where a greater dependence would translate into a greater dose reduction between full-field and VOI protocols. It can be anticipated that the 2.35 MV/carbon beam
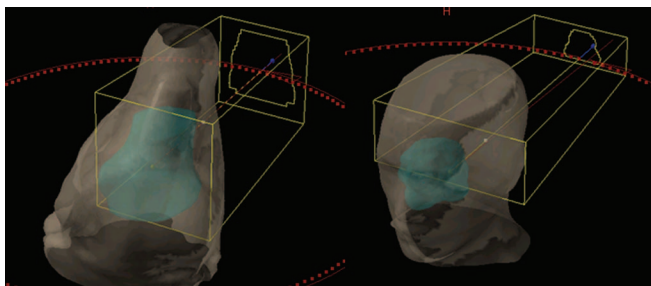
should show a larger variation of S_{total} with field size compared to therapeutic beams due to its softer energy spectrum and increased contribution of lateral scatter. S_{total} was quantified through ionization chamber measurement (PTW Semiflex, 31010, 0.125 cc) at depth 10 cm in water, SAD 100 cm, for jaw-defined square field sizes ranging 2 $\times$ 2 cm^2 to 25 $\times$ 25 cm^2. For comparison, these measurements were repeated for a therapeutic 6 MV beam.

Additional measurements were performed to demonstrate the dose distribution, both inside and outside of the VOI, for exemplary 2.35 MV/carbon CBCT acquisitions, compared to the full-field approach. An array of thermoluminescent dosimeters (TLDs) was used to sample a 1D dose profile during VOI CBCT imaging, after defining a VOI with dimensions $9 \times 8 \times 6$ cm^3 encompassing the ethmoid and sphenoid sinuses of an anthropomorphic head phantom (Fig. 3, right). Lithium borate (Li$_2$B$_4$O$_7$:Mn) TLDs were used for their effective atomic number (Zeff = 7.4) and relative low energy dependence (with a response ratio of 0.9:1 for 30 keV:1.25 MeV). TLDs were placed along the anterioposterior axis in a cranial anthropomorphic phantom and located in regions both inside and outside of the VOI, as shown in Fig. 4. In the same phantom, EBT2 Gafchromic film (International Specialty Products, Inc.) was positioned just above the phantom slice containing the TLDs (and ~ 1 cm above the superioinferior location of the TLD crystals). The EBT2 film was calibrated with multiple exposures of known doses in the range of the imaging dose and digitized using a flatbed film scanner (Epson 10000XL) according to the film manufacturer's recommendations. The red channel of acquired 48-bit color images was calibrated to dose in cGy, while the blue channel was used for compensation of film nonuniformity and artifacts.[21]

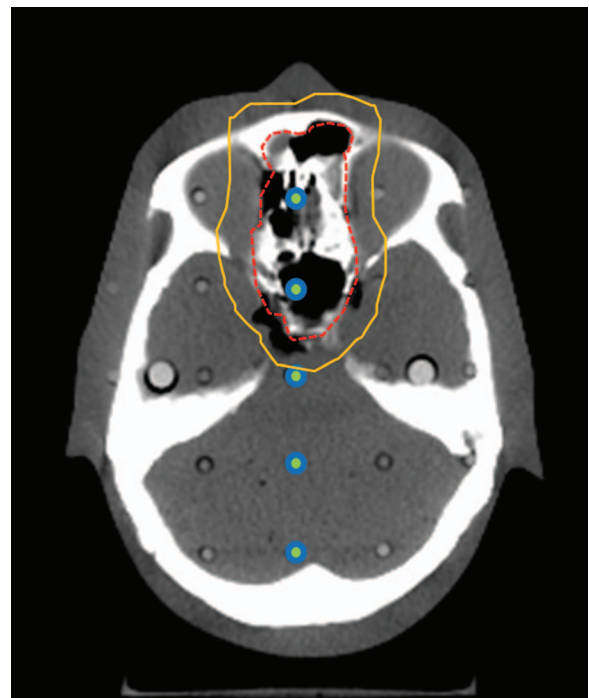FIG. 3. VOIs defined in the lamb head (left) and human cranial phantom (right).

FIG. 4. Example PTV (inner contour, dashed), VOI (outer contour, solid) and locations of TLDs (circles).
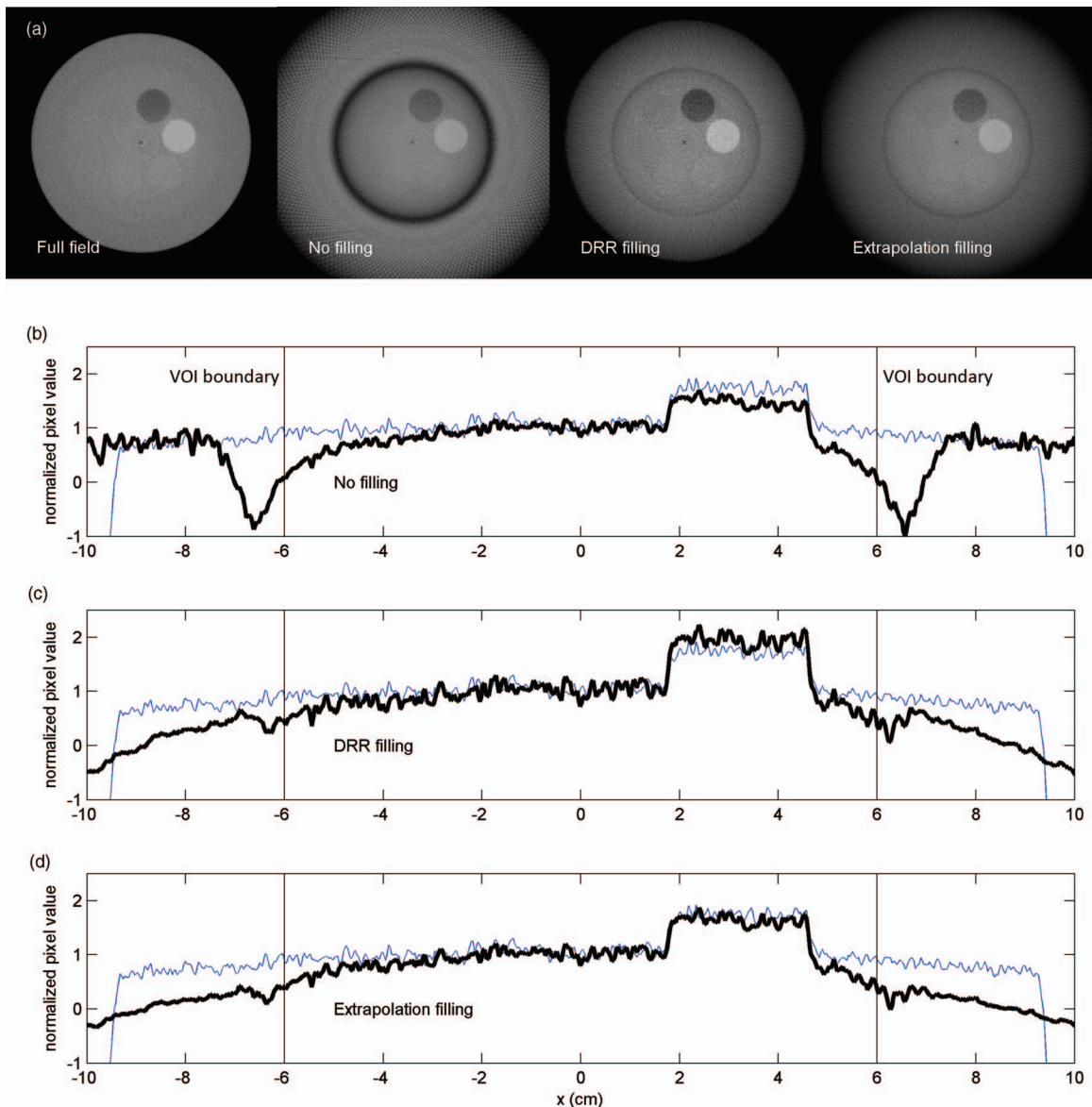
FIG. 5. (a) Comparison of axial images from the full-field acquisition, reconstruction without prior projection filling, and reconstruction with prior DRR-filling or extrapolation of truncated projection data. Horizontal profiles through these images are shown comparing results (b) without projection filling, (c) with DRR filling and (d) extrapolation-based methods. Profiles are shown in comparison to the corresponding full-field acquisition profile (thin line).

For the same phantom setup and both dosimeters, separate measurements were made with: (i) a full-field protocol with a fixed field size of 23 cm × 30 cm and (ii) the VOI technique, wherein the MLC tracked the off-axis sinus VOI. For both dosimeters, in order to deliver an imaging dose within the dynamic range (∼15–20 cGy in the VOI), the imaging protocol was repeated multiple times.

II.G. Dependence of CNR on VOI dimension

With a scatter-to-primary ratio (SPR) typically below 0.3, standard therapeutic MV x-ray beams exhibit only a modest variation (e.g., <10%) of CNR over a wide range of field size.[10] However, given that low-Z target beams exhibit a much softer energy spectrum, potentially containing more than 50% of photons in the diagnostic energy range,[2,13] it was of interest

here to examine whether CNR increases with decreased aperture size in VOI CBCT imaging. To allow imaging with small VOI dimensions, a "mini-CNR" phantom was constructed. This was comprised of a 28 mm-diameter cylinder, composed of simulated lung ($\rho_e^w = 0.29$), water ($\rho_e^w = 1.00$), and cortical bone ($\rho_e^w = 1.69$) materials stacked vertically along the axis of an 18 cm diameter cylindrical water phantom. The three materials were arranged in proximity such that they could be encompassed entirely by a 4×4 cm^2 projected field. 2.35 MV/carbon VOI CBCT was performed with cylindrical VOIs of diameters of 4, 6, 8, 10, 12, and 15 cm, and images were reconstructed with 3 mm slice thickness and prior DRR filling. For each field size, the dose to the center of the VOI volume was maintained at 2.5 cGy by adjusting the cMUs per projection. CNR was calculated for bone and lung relative to water background (BG), using CNR = $(P_{ROI} - P_{BG})/(\sigma^2_{ROI}$
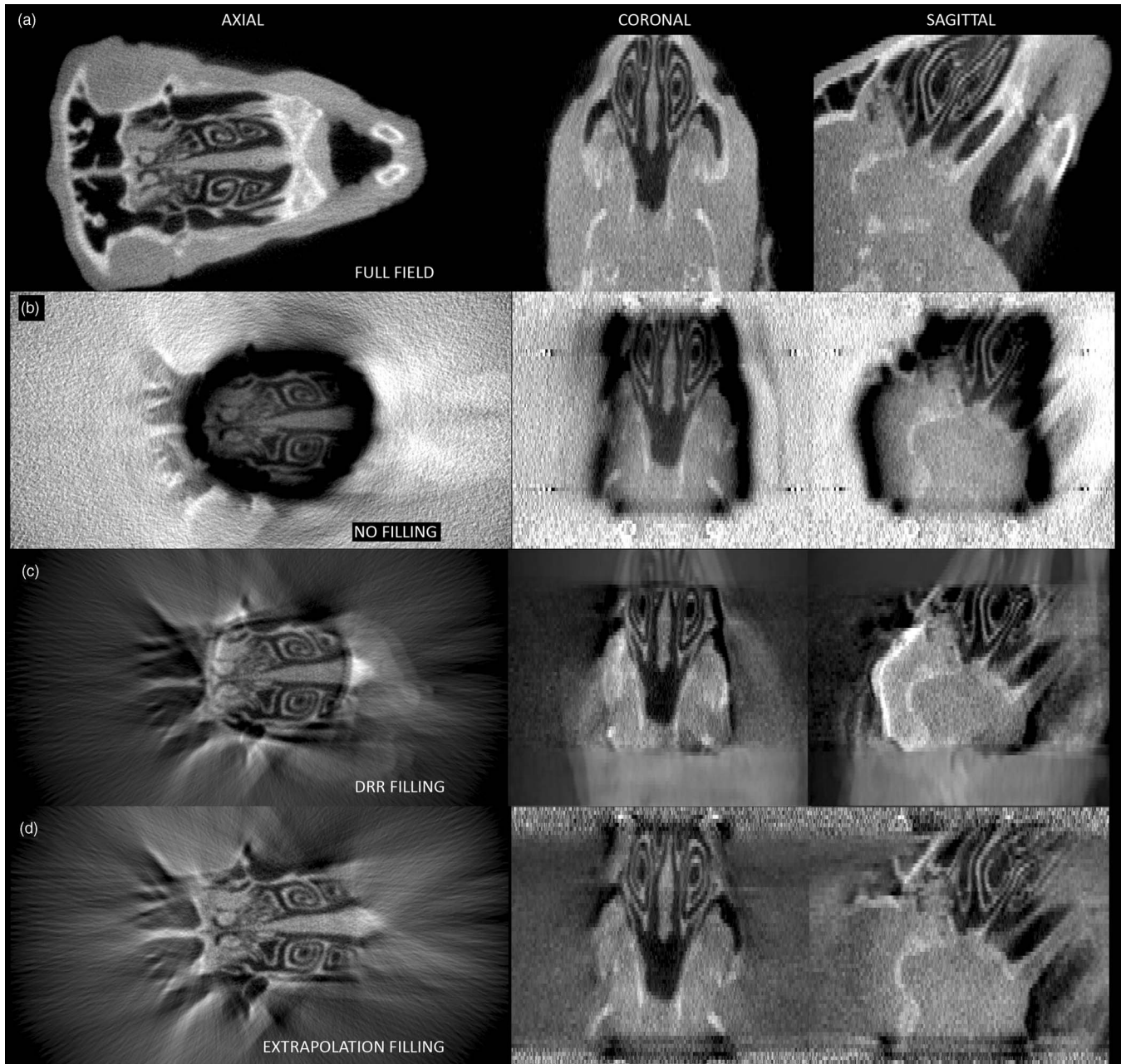
FIG. 6. Views through reconstructed 2.35 MV/carbon CBCT image data of the lamb head, showing the result of (a) full-field acquisition, (b) VOI reconstruction without projection filling, (c) with prior DRR filling, and (d) extrapolation of truncated projection data.

$+ \sigma^2_{BG})^{0.5}$, where P and σ are the mean and standard deviation of voxel value in 1.0 cm diameter circular regions of interest (ROIs). To estimate uncertainty in this value, CNR was obtained from seven consecutive slices and the mean and standard deviation were calculated.

III. RESULTS AND DISCUSSION

III.A. Reconstruction with DRR filling

Figure 5 shows reconstructed images of the cylindrical phantom, comparing the full-field and VOI protocols, and demonstrating the effects of either the DRR filling or extrapolation methods. The images shown correspond to a dose of

3 cGy at the middle of the cylinder (0.13 mGy per projection) and were reconstructed with 2 mm slice thickness. Reconstruction using the raw, unfilled projections compromises image uniformity, and as shown in horizontal profiles through the image slices, the boundary artifact occupies a 2–3 cm wide ring around the inner circumference of the VOI. DRR filling of truncated projections largely eliminates this artifact, but within ~1 cm of the periphery, there remains a slight loss of uniformity. It is notable that the extrapolation method achieves approximately the same level of artifact reduction as the DRR filling approach, which raises the question of the relative computational efficiency of the two methods. For the images shown in Fig. 5, without filling or extrapolation of projections, the MATLAB-based reconstruction required ~1.5

min (using Intel Core2 Extreme Q9300 at 2.54 GHz). With our present implementation, the DRR filling method increases this time by a factor of 4.2 on average, while the extrapolation method increases reconstruction time by a factor of 2. Our present reconstruction code, while flexible, is not optimized for speed, and we anticipate that the times for reconstruction should not be prohibitive in either case, since reconstruction may be expedited substantially through optimization, compilation, or distributed processing using, e.g., a graphics processing unit (GPU).

With regard to artifact reduction, Fig. 6 shows similar effects in the images of the lamb head-and-neck, demonstrating the boundary artifact in three dimensions. (Note that the image information outside of the VOI in all dimensions is superfluous and could be masked to improve clarity, but is included here for completeness.) The full-field images were acquired with a dose of ~3.5 cGy at midseparation of the cranium, i.e., 0.15 mGy per projection. The VOI acquisition was done with the same cMU setting per projection. As for the cylindrical phantom, the DRR filling method reduces the boundary artifact and also improves the apparent cupping effect within the VOI. At several locations surrounding the VOI, however, localized high intensity boundary artifacts remain. Investigation of the cause revealed that particular regions of a subset of projections showed discontinuities at the truncated projection/DRR boundary, evidently caused by the limitation of the linear fit used to match the DRR and projection data as described above. This occurred, for example, where a projection extended beyond the external surface into air. In principle, steps outlined in Fig. 2 could be refined: rather than simply scaling one data set according to a linear fit, region-specific intensity matching could be performed. The extrapolation-based method produced comparable results, but with slightly improved boundary artifacts, presumably due to the explicit matching of the extrapolation at the truncation boundary, as specified in Eqs. (1) and (2). The results of the extrapolation method are consistent with previous findings, for example, linear extrapolation of truncated projections was done by Ford *et al.* for 6 MV, for MLC-collimated projection images, yielding acceptable results in VOIs as small as 8 cm in dimension.[12] In summary, while the DRR filling method was inspired by previous work by MacDonald[17] and Kadrmas[16] in its use of pre-existing patient data, at least for objects imaged here, it does not appear to present obvious advantages in minimizing truncation artifacts.

III.B. Dose reduction with low-Z VOI CBCT

As expected, the 2.35 MV/carbon beam exhibits a greater dependence of total scatter factor with field size, relative to 6 MV (Fig. 7). This comparison underlines a particular advantage of the VOI approach when combined with the low-Z target beam. As an example, for a large (i.e., "full-scatter") subject, compared to full-field imaging (e.g., with a 25×25 cm^2 field), reducing the field size with a VOI aperture to 4×4 cm^2 would yield a 39% reduction in the dose for the 2.35 MV/carbon beam, compared to a 23% reduction at 6 MV. With respect to dose reduction inside the VOI, the benefit of
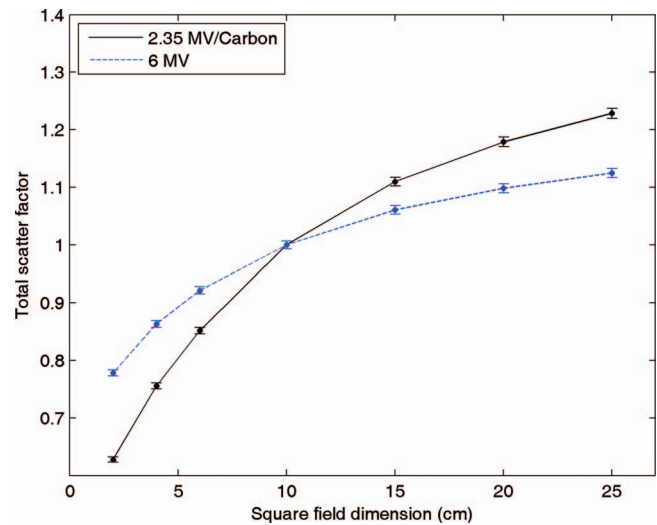

FIG. 7. Measured total scatter factor (S_{total}) data, comparing the 2.35 MV/carbon and 6 MV beams.

beam collimation should increase as the quality of the low-Z target beam is reduced—with the greatest advantage realized for kV x-ray imaging. For example, Chen *et al.* demonstrated that an 80 kVp beam, collimated by a 2.4 cm diameter copper mask during CBCT acquisition, reduced the dose *inside* the VOI by almost a factor of five.[11]

Figure 8 shows the distribution of relative dose, across the anterioposterior dimension of the human head phantom, for full-field and VOI protocols. At distances beyond 5 cm from the posterior aspect of the VOI, the dose is reduced to ~25%–30% of the full-field value. Inside the VOI, the full-field acquisition delivers higher dose than the VOI method, and this difference is as large as 15% within the volume. Where the VOI extended beyond the anterior surface, the surface dose was essentially equivalent between the VOI and full-field scans. However, at the posterior surface of the cranium, well outside of the imaged volume, the VOI method
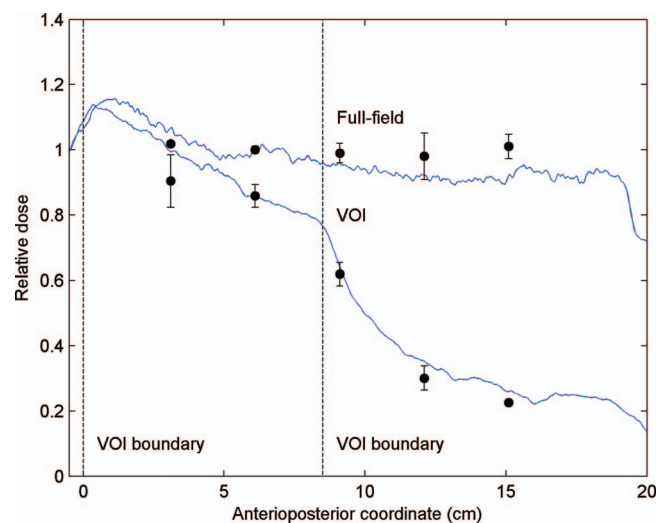

FIG. 8. Relative dose along the anterioposterior axis of the head phantom, measured using EBT2 Gafchromic film (line) and TLDs (points).
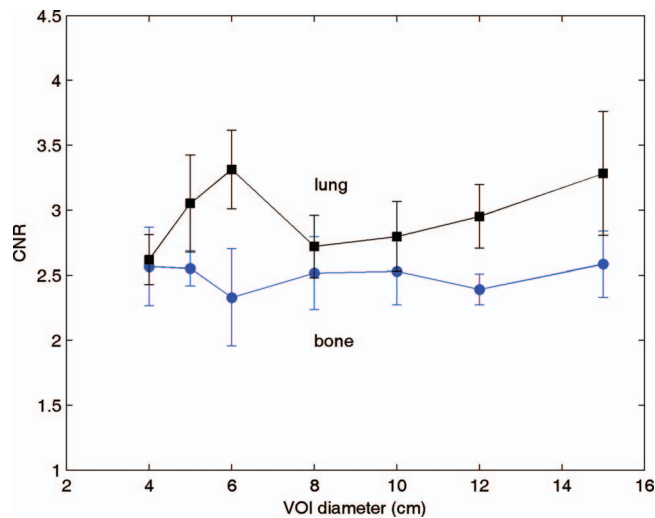
FIG. 9. Measured CNR for cortical bone and lung, as a function of field size, for square fields ranging in dimension from 4×4 cm^2 to 15×15 cm^2.

reduced the surface dose by a factor greater than 4. Some discrepancy between the TLD and EBT2 measurements is apparent; however, this can be expected given the uncertainty of the TLD measurements (calculated from multiple TLD readings and indicated in the figure), and the EBT2 film (which we estimate from multiple trials to be $\sim\pm5\%$) for the low doses measured during the imaging acquisition.

III.C. CNR in low-Z VOI CBCT

Figure 9 shows measured CNR for lung and bone relative to water as a function of cylindrical VOI diameter. Within the uncertainty of the measurement, no systematic dependence of CNR is apparent with field size. This suggests that the scatter-to-primary ratio of the 2.35 MV/carbon beam is sufficiently low to cause CNR to be insensitive to the dimension of the collimation used. This situation is substantially different from VOI CBCT with diagnostic energy x-ray beams for which the scatter to primary ratio is much higher; for example, Chen *et al.* observed a 45% increase in CNR with the VOI method, relative to full-field imaging, at 80 kVp.[11] For the 2.35 MV/carbon beam used here, the results in Fig. 9 suggest that while there is little benefit in reducing VOI dimension from a CNR standpoint, CNR is not degraded inside even small (e.g., 4 cm diameter) VOIs. In summary, the results presented here indicate that the value of the VOI method is dose reduction outside of the VOI, not improvement of CNR.

IV. CONCLUSIONS

This study has demonstrated proof-of-concept of a VOI CBCT technique using an x-ray beam produced by 2.35 MeV electrons incident on a carbon linac target. The workflow presented links the treatment planning process with the imaging technique, allowing the imaging protocol (i.e., including VOI shape, location, and arc length) to be set by the treatment planner according to the particular geometry of the patient.

We anticipate further work to focus on yet unaddressed steps of Fig. 1, for example, calculation of the 2.35 MV/carbon imaging dose within the planning system, use of more versatile MLC and arc sequences, and assessment of the accuracy of coregistration of VOI image data with reference CT sets. FDK reconstruction, without compensating for missing data outside of truncated projections, produces boundary artifacts, $\sim$2–3 cm wide, obscuring useful image data inside the VOI. As demonstrated in VOI CBCT images of a cylindrical phantom and a lamb head-and-neck section, these artifacts, as well as cupping inside the VOI, can be improved substantially by filling using *a priori* image data from DRRs generated from the planning CT set, or by extrapolating the truncated image data. Compared to 6 MV, the 2.35 MV/carbon beam shows a greater dependence of total scatter factor on field size, indicating a greater possible benefit of the VOI technique for low-Z target beam with regard to reducing the dose inside the VOI itself. Dosimetric measurements in an anthropomorphic head phantom demonstrate a dose reduction by up to 15% and 75% inside the VOI and 5 cm from the VOI boundary, respectively, compared to full-field imaging. For the 2.35 MV/carbon beam, CNR was shown to be approximately constant with VOI dimension. In summary, the technique appears to be viable, combining the useful imaging characteristics of the low-Z target beam with the capacity to localize imaging dose to the anatomy relevant to the image guidance task.

[a] Author to whom correspondence should be addressed. Electronic mail: james.robar@cdha.nshealth.ca

[1] T. Connell and J. L. Robar, "Low-Z target optimization for spatial resolution improvement in megavoltage imaging," Med. Phys. **37**, 124–131 (2010).

[2] E. J. Orton and J. L. Robar, "Megavoltage image contrast with low-atomic number target materials and amorphous silicon electronic portal imagers," Phys. Med. Biol. **54**, 1275–1289 (2009).

[3] B. A. Faddegon, V. Wu, J. Pouliot, B. Gangadharan, and A. Bani-Hashemi, "Low dose megavoltage cone beam computed tomography with an unflattened 4 MV beam from a carbon target," Med. Phys. **35**, 5777–5786 (2008).

[4] B. A. Faddegon, M. Aubin, A. Bani-Hashemi, B. Gangadharan, A. R. Gottschalk, O. Morin, D. Sawkey, V. Wu, and S. S. Yom, "Comparison of patient megavoltage cone beam CT images acquired with an unflattened beam from a carbon target and a flattened treatment beam," Med. Phys. **37**, 1737–1741 (2010).

[5] D. A. Roberts, V. N. Hansen, A. C. Niven, M. G. Thompson, J. Seco, and P. M. Evans, "A low Z linac and flat panel imager: Comparison with the conventional imaging approach," Phys. Med. Biol. **53**, 6305–6319 (2008).

[6] D. A. Roberts, V. N. Hansen, M. G. Thompson, G. Poludniowski, A. Niven, J. Seco, and P. M. Evans, "Comparative study of a low-Z cone-beam computed tomography system," Phys. Med. Biol. **56**, 4453–4464 (2011).

[7] D. Sawkey, M. Lu, O. Morin, M. Aubin, S. S. Yom, A. R. Gottschalk, A. Bani-Hashemi, and B. A. Faddegon, "A diamond target for megavoltage cone-beam CT," Med. Phys. **37**, 1246–1253 (2010).

[8] J. L. Robar, T. Connell, W. Huang, and R. G. Kelly, "Megavoltage planar and cone-beam imaging with low-Z targets: Dependence of image quality improvement on beam energy and patient separation," Med. Phys. **36**, 3955–3963 (2009).

[9] E. K. Breitbach, J. S. Maltz, B. Gangadharan, A. Bani-Hashemi, C. M. Anderson, S. K. Bhatia, J. Stiles, D. S. Edwards, and R. T. Flynn, "Image quality improvement in megavoltage cone beam CT using an imaging beam line and a sintered pixelated array system," Med. Phys. **38**, 5969–5979 (2011).

[10] D. A. Jaffray, J. J. Battista, A. Fenster, and P. Munro, "X-ray scatter in megavoltage transmission radiography: Physical characteristics and influence on image quality," Med. Phys. **21**, 45–60 (1994).

[11] L. Chen, C. C. Shaw, M. C. Altunbas, C. J. Lai, X. Liu, T. Han, T. Wang, W. T. Yang, and G. J. Whitman, "Feasibility of volume-of-interest (VOI) scanning technique in cone beam breast CT: A preliminary study," Med. Phys. **35**, 3482–3490 (2008).

[12] E. C. Ford, J. Chang, K. Mueller, K. Sidhu, D. Todor, G. Mageras, E. Yorke, C. C. Ling, and H. Amols, "Cone-beam CT with megavoltage beams and an amorphous silicon electronic portal imaging device: Potential for verification of radiotherapy of lung cancer," Med. Phys. **29**, 2913–2924 (2002).

[13] J. L. Robar, "Generation and modelling of megavoltage photon beams for contrast-enhanced radiation therapy," Phys. Med. Biol. **51**, 5487–5504 (2006).

[14] L. A. Feldkamp, L. C. Davis, and J. W. Kress, "Practical cone-beam algorithm," J. Opt. Soc. Am. A **1**, 612–619 (1984).

[15] K. Ogawa, M. Nakajima, and S. Yuta, "A reconstruction algorithm from truncated projections," IEEE Trans. Med. Imaging **3**, 34–40 (1984).

[16] D. J. Kadrmas, R. J. Jaszczak, J. W. McCormick, R. E. Coleman, and C. B. Lim, "Truncation artifact reduction in transmission CT for improved SPECT attenuation compensation," Phys. Med. Biol. **40**, 1085–1104 (1995).

[17] A. O. MacDonald, "Investigation of megavoltage volume-of-interest cone-beam computed tomography," M.S. thesis (Dalhousie University, 2010).

[18] R. Chityala, K. R. Hoffmann, S. Rudin, and D. R. Bednarek, "Region of interest (ROI) computed tomography (CT): Comparison with full field of view (FFOV) and truncated CT for a human head phantom," Proc. Soc. Photo-Opt. Instrum. Eng. **5745**, 583–590 (2005).

[19] L. Yu, Y. Zou, E. Y. Sidky, C. A. Pelizzari, P. Munro, and X. Pan, "Region of interest reconstruction from truncated data in circular cone-beam CT," IEEE Trans Med Imaging **25**, 869–881 (2006).

[20] K. J. Ruchala, G. H. Olivera, J. M. Kapatoes, P. J. Reckwerdt, and T. R. Mackie, "Methods for improving limited field-of-view radiotherapy reconstructions using imperfect a priori images," Med. Phys. **29**, 2590–2605 (2002).

[21] A. Micke, D. F. Lewis, and X. Yu, "Multichannel film dosimetry with nonuniformity correction," Med. Phys. **38**, 2523–2534 (2011).